



ALMA MATER STUDIORUM
UNIVERSITÀ DI BOLOGNA

ARCHIVIO ISTITUZIONALE
DELLA RICERCA

Alma Mater Studiorum Università di Bologna Archivio istituzionale della ricerca

Thiolate end-group regulates ligand arrangement, hydration and affinity for small compounds in monolayer-protected gold nanoparticles

This is the final peer-reviewed author's accepted manuscript (postprint) of the following publication:

Published Version:

Pellizzoni E., Sologan M., Daka M., Pengo P., Marson D., Posel Z., et al. (2022). Thiolate end-group regulates ligand arrangement, hydration and affinity for small compounds in monolayer-protected gold nanoparticles. JOURNAL OF COLLOID AND INTERFACE SCIENCE, 607(Pt 2), 1373-1381 [10.1016/j.jcis.2021.09.083].

Availability:

This version is available at: <https://hdl.handle.net/11585/858701> since: 2022-02-15

Published:

DOI: <http://doi.org/10.1016/j.jcis.2021.09.083>

Terms of use:

Some rights reserved. The terms and conditions for the reuse of this version of the manuscript are specified in the publishing policy. For all terms of use and more information see the publisher's website.

This item was downloaded from IRIS Università di Bologna (<https://cris.unibo.it/>).
When citing, please refer to the published version.

(Article begins on next page)

This is the final peer-reviewed accepted manuscript of:

Journal of Colloid and Interface Science 2022, 607, 1373 - 1381

The final published version is available online at:

<https://doi.org/10.1016/j.jcis.2021.09.083>

Terms of use:

Some rights reserved. The terms and conditions for the reuse of this version of the manuscript are specified in the publishing policy. For all terms of use and more information see the publisher's website.

This item was downloaded from IRIS Università di Bologna (<https://cris.unibo.it/>)

When citing, please refer to the published version.

1 **Thiolate end-group regulates ligand arrangement, hydration and**
2 **affinity for small compounds in monolayer-protected gold**
3 **nanoparticles**
4
5

6 *Elena Pellizzoni,^{a,1} Maria Şologan,^a Mario Daka,^a Paolo Pengo,^a Domenico Marson,^{b,1} Zbyšek*
7 *Posel,^{b,c} Stefano Franchi,^{d,2} Luca Bignardi,^e Paola Franchi,^f Marco Lucarini,^{f,*} Paola Posocco,^{b,*}*
8 *and Lucia Pasquato^{a,*}*
9

10
11 ^aDepartment of Chemical and Pharmaceutical Sciences and INSTM Trieste Research Unit,
12 University of Trieste, 34127 Trieste (Italy)

13 ^bDepartment of Engineering and Architecture, University of Trieste, 34127 Trieste (Italy)

14 ^cDepartment of Informatics, Jan Evangelista Purkyně University, 400 96 Ústínad Labem (Czech
15 Republic)

16 ^dElettra Sincrotrone Trieste S.C.p.A., 34149 Trieste (Italy)

17 ^eDepartment of Physics, University of Trieste, 34127 Trieste (Italy)

18 ^fDepartment of Chemistry “G. Ciamician”, University of Bologna, I-40126 Bologna (Italy)
19
20
21
22
23

24 ¹These authors contributed equally to the work.

25
26 ²Present address: Consiglio Nazionale delle Ricerche - Istituto di Struttura della Materia 00133
27 Roma – Italy

28
29 *Corresponding author

30 E-mail address: marco.lucarini@unibo.it; paola.posocco@dia.units.it; lpasquato@units.it.
31
32
33
34
35
36
37
38

39 **Abstract**

40 The ability to control the properties of monolayer protected gold nanoparticles (MPNPs) discloses
41 unrevealed features stemming from collective properties of the ligands forming the monolayer and
42 presents opportunities to design new materials. To date, the influence of ligand end-group size and
43 capacity to form hydrogen bonds on structure and hydration of small MPNPs (< 5 nm) has been
44 poorly studied. Here, we show that both features determine ligands order, solvent accessibility,
45 capacity to host hydrophobic compounds and interfacial properties of MPNPs. The polarity
46 perceived by a radical probe and its binding constant with the monolayer investigated by electron
47 spin resonance is rationalized by molecular dynamics simulations, which suggest that larger space-
48 filling groups – trimethylammonium, zwitterionic and short polyethylene glycol – favor a radial
49 organization of the thiolates, whereas smaller groups – as sulfonate – promote the formation of
50 bundles. Zwitterionic ligands create a surface network of hydrogen bonds, which affects
51 nanoparticle hydrophobicity and maximize the partition equilibrium constant of the probe. This
52 study discloses the role of the chemistry of the end-group on monolayer features with effects that
53 span from molecular- to nano-scale and opens the door to a shift in the conception of new MPNPs
54 exploiting the end-group as a novel design motif.

55

56 **Keywords:** Nanochemistry, Supramolecular Chemistry, Electron Spin Resonance, Molecular
57 Simulations, MD, Weak Interactions, Hydrophobic Binding.

58

59 **1. Introduction**

60 The simultaneous control of topology and solvation of functional groups in a catalytic site is
61 achieved in natural systems with proper folding of the proteic polymer.^[1] This has significant
62 influence on cell-protein interaction,^[2,3] internalization mechanisms,^[4,5] recognition^[6] and
63 catalytic processes,^[7] to mention a few. In an attempt to mimic Nature's "machines" scientists
64 have turned their attention to synthetic models such as micelles^[8] or liposomes.^[9-13] Metal
65 nanoparticles (NPs) coated by organic monolayers of self-assembling ligands (SAMs) have also
66 been studied as protein-mimicking, catalytic artificial systems by exploiting their inherent
67 multivalence, cooperativity, nanoconfinement, and control achieved in their preparation.^[14-16]
68 Indeed, properties of SAM-NPs can be modulated by a variety of parameters^[17-22] such as ligand
69 chemistry, functional groups exposed on the surface, nanoparticle dimension, ligand length and
70 density, molecular composition of the monolayer, and ligand organization for heteroligand
71 shells.^[23-25] All these parameters impact on the activity of NPs and the way they interact with
72 solvent^[26,27] and external (biological) environment.^[28-33]

73 Ligand end group chemistry is a key element able to impart to the nanoparticles specific ability,
74 properties, controlled colloidal stability and dispersibility.^[33] Yet, studies aimed to rationalize this
75 effect on monolayer structure and ligand environment are isolated and a general framework lacks.
76 This is particularly relevant for small and ultrasmall NPs – namely below 5 nm – where *i*) the high
77 surface curvature impacts more on ligand arrangement than in larger NPs, which rather resemble
78 2-D SAM and *ii*) the surface chemistry plays a central role in regulating the transient bionano
79 interactions with proteins and cell membranes.^[31,32] The lack of studies on ligand end group effect
80 is partially due to the difficulty in characterizing the monolayer structure. In the solid state
81 information about the organization of the shell is retrieved from X-Ray structure analysis of small
82 gold clusters/nanoparticles,^[34-36] protected by ligands designed to impart rigidity to the SAMs and

83 presenting relatively short alkyl chains and/or aromatic rings. However, this cannot be extended
84 to larger NPs functionalized by flexible and longer thiolates. Thus, probing ligand distribution in
85 solution on larger NPs is still extremely challenging.^[37]

86 As indeed stated by Grzybowski recently, “*we have only an indirect understanding (from*
87 *simulations) of how the ligand shell is organized*”.^[33] For instance, Glotzer described the influence
88 of alkanethiolate chain length, temperature and nanoparticle size on ligand arrangement.^[38] Below
89 450 K, molecular dynamics (MD) calculations suggest long-range ordering of thiolates having
90 more than 9 carbon atoms. They form clusters (e.g. bundles), similar to those of alkanethiols on
91 flat Au(111) surfaces, but with larger tilting angles. For longer chain lengths (9 and 17 carbons)
92 Grest^[39] reported on the effect of the end group (CH₃, NH₂, COOH) and its ionization state on the
93 structure of gold NPs (AuNPs) coated with ω-functionalized alkylthiolates in water and decane.
94 This analysis was later expanded by Sphor^[40] for AuNPs coated with 6 to 24 carbon atom long
95 chains, linear and branched. Both computational studies supported a chain length dependence of
96 the hydrophobic bundling and a negligible influence of the head group chemistry. Repulsion
97 between charged chains seems to mitigate ligand association and favours more disordered
98 conformations.

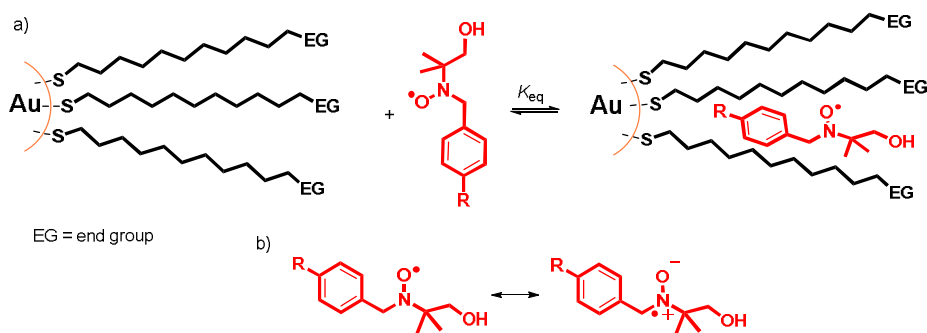
99 Coupling indirect experimental approaches with theoretical or computational models has been of
100 help in overcoming such limitations.^[41-43] In a recent work by Murphy,^[19] the combination of NMR
101 and implicit solvent MD simulations suggests that monolayers of (16-
102 mercaptohexadecyl)trimethylammonium bromide on AuNPs organize in a radial fashion
103 (following the continuous model introduced by Landman^[44,45]) with end groups more closely
104 packed in larger than in smaller (< 10 nm) NPs. Nonetheless, the divergent mode of ligand
105 organization – radial vs. bundled – on metal NP surface has not found a rational harmonization in

106 literature and the definition of which aspects direct ligand ordering toward a specific arrangement
107 has not fully emerged.

108 Solvation energy contribution to SAM organization needs to be considered, especially when there
109 are polar end groups that strongly interact with the solvent molecules,^[41] or charged groups as
110 ammonium ions, carboxylates and sulfonates which may be involved in hydrogen bonds.
111 Moreover, for instance, primary ammonium ions differ from quaternary ones in size, charge
112 density, hydrophilicity and consequently in solvation by water. Additionally, solvent may screen
113 out inter-particle attractive interactions leading to monolayers interdigitation, which in turn is
114 accompanied by a change in the conformational structure of the ligands.^[46-48]

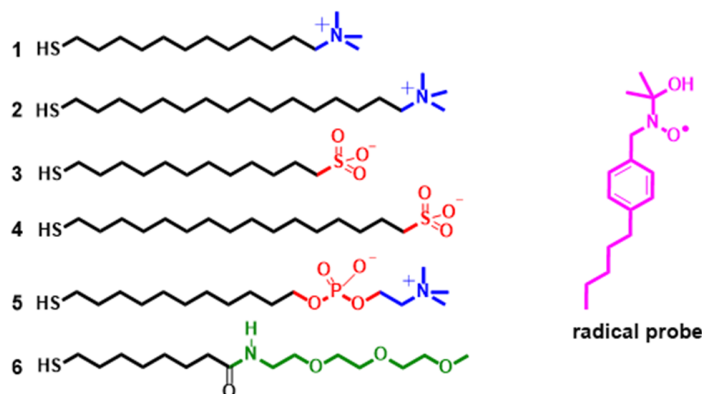
115 Different ligand arrangements mean also different accessibility of solvent and small molecules
116 to the inner of the monolayer. Monolayer accessibility is relevant for sensing^[49-53] and drugs
117 binding by weak interactions^[54,55] and can be addressed by species sensitive to the polarity of the
118 environment that become good reporters of the hydrophobicity/hydrophilicity of their local
119 surroundings. This is the case of specific radical probes with affinity for the monolayer and whose
120 spectroscopic parameters are influenced by the local environment, thus enabling to gather
121 information about the polarity of the medium by electron spin resonance (ESR) spectra analysis.
122 ESR spectroscopy allows the assessment of the partition equilibrium constant, K_{eq} , of radical
123 probes between monolayer and solvent (**Figure 1**), and the spectroscopic parameters are directly
124 related to the to the hydrophobicity of the medium.^[56,57]

125 In this work, ESR measurements are carried out using the radical probe drawn in **Figure 2**, which
126 has a good affinity for hydrophobic monolayers and whose spectroscopic parameters strictly
127 depend from the local polarity of the surrounding medium and the monolayer.^[41,42,49,56-58]



128
 129
 130 **Figure 1.** a) Partition equilibrium of a radical probe between water and NP monolayer; b)
 131 mesomeric forms of the radical probe: on the left, the one prevalent in hydrophobic media and on
 132 the right, that prevalent in hydrophilic media.

133



134
 135 **Figure 2.** Structure of ligands 1–6 used for the preparation of homoligand monolayer-protected
 136 AuNPs (NP1-NP6) and the radical probe used in this study.

137
 138 ESR spectra, carried out at different temperatures, are analyzed and simulated to determine the
 139 hyperfine coupling constants, which are here coupled with MD calculations of NPs to rationalize
 140 monolayer structure, solvation, and probe location. ESR measurements at different nanoparticle
 141 concentration allow deriving the equilibrium constants of the probe free in solution and within the
 142 monolayer, which is an indication of the host properties of the monolayer. Selected NPs are

143 characterized by synchrotron-based X-ray photoelectron spectroscopy (XPS), in order to estimate
144 the thickness of the self-assembled monolayer and to compare it with data from MD simulations.

145 We chose ligands, well known in the literature of SAMs, presenting as terminal groups: a positive
146 charged quaternary ammonium ion, ligands **1** and **2**, with alkyl chain of 12 and 16 carbon atoms,
147 respectively, indicated as C12 and C16; a negatively charged sulfonate ion, ligands **3** and **4**, with
148 chains C12 and C16, respectively; a zwitterionic group having an inner phosphate and an ending
149 trimethylammonium group, ligand **5**, and a neutral triethylene glycol monomethyl ether, ligand **6**
150 (**Figure 2**). The thiolates were designed to differ in nature and size of the end-groups as well as in
151 chain length. The gold core diameter, of ~ 4 nm, was selected because of the relevance of the
152 surface chemistry at this size for the interactions with biological entities and was maintained as
153 much as possible constant. In principle, the dimension of NP core (relative to the ligand length)
154 may itself affect the shell organization; lowering the diameter, the chains gain available free
155 volume due to the increased core surface curvature. This reduces the chance of interchain
156 interactions, making ligand clustering more difficult and thus affecting the overall monolayer
157 structure.

158 The results from this systematic investigation allows us to draw general conclusions on the role
159 of surface group chemistry on ligand arrangement, monolayer hydration and ability to complex
160 small hydrophobic compounds.

161

162 **2. Materials and methods**

163 *Synthesis*: Thiols **1**, and **3** were prepared as reported in literature.^[59] Detailed procedures for the
164 preparation of thiols **2**, **4**, and **5** and their characterization are described in Supporting Material
165 (SM).

166 The procedure used for the preparation of gold NPs was adapted from ref. 60.^[60] The experimental
167 conditions used for the syntheses of **NP1-NP5** are the same and in particular the reactions were
168 carried out at room temperature with a ratio between HAuCl_4 : TOAB : NaBH_4 of 1 : 5.4 : 14.5 on
169 a scale of 0.100 g, 0.296 mmol, of HAuCl_4 or half of this for **NP3**.

170 *Synthesis of NP1:* To a solution of tetrachloroauric acid (0.100 g, 0.296 mmol, 1 equiv) in 11.6
171 mL deoxygenated milliQ water, TOAB (0.869 g, 1.59 mmol, 5.4 equiv) in 8.8 mL of deoxygenated
172 chloroform was added and the solution was let to stir for 30 min at room temperature. The two
173 phases were separated and a solution of sodium borohydride (0.161 g, 4.27 mmol, 14.5 equiv) in
174 7.8 mL milliQ water was added to the organic phase and the reaction mixture stirred for 15 minutes
175 under argon atmosphere. After this time a solution of **1** (0.010 g, 0.034 mmol) in 6 mL isopropanol
176 was added and the nanoparticles precipitated. After 1.2 h the solid was separated and the
177 nanoparticles were washed six times with chloroform (6 x 15 mL) (4500 rpm, 4 min, 25 °C). TEM:
178 4.4 ± 1 nm, $n = 495$. DLS: $D_H 7.97 \pm 1.98$ nm. TGA 15 %. Average composition: $\text{Au}_{2950}\text{C}_{12}\text{N}_{385}$.

179 *Synthesis of NP2:* A solution of TOAB (0.868 g, 1.59 mmol, 5.4 eq) in 9 mL of chloroform was
180 added under argon atmosphere to an aqueous solution of tetrachloroauric acid (0.100 g, 0.296
181 mmol, 1 eq) in 11.6 mL milliQ water at 25 °C and the reaction was let to stir for 15 minutes. The
182 two phases were separated and a solution of sodium borohydride (0.161 g, 4.27 mmol, 14.5 eq) in
183 7.8 mL of water was added to the organic phase. The red colored solution was stirred for 15
184 minutes and then a solution of **2** (0.015 g, 0.042 mmol) in 8.2 mL of isopropanol was added. Under
185 these conditions the nanoparticles precipitated and the dispersion was stirred for 2 hours. The solid
186 was separated and washed with chloroform (5 x 30 mL, 4500 rpm, 5 min). TEM: 4.2 ± 0.9 nm (n
187 = 307). DLS: $D_H 7.66 \pm 2.10$ nm. TGA 16%. Average composition: $\text{Au}_{2759}\text{C}_{16}\text{N}_{326}$.

188 *Synthesis of NP3*: $\text{HAuCl}_4 \cdot x\text{H}_2\text{O}$ (0.050 g, 0.147 mmol, 1 eq) was dissolved in 5.8 mL of
189 deoxygenated water and stirred for 30 min at room temperature with a solution of TOABr (0.435
190 mg, 0.795 mmol, 5.4 eq) in 4.4 mL of deoxygenated chloroform. The colorless aqueous layer was
191 discarded, while the orange organic phase containing the gold ions was placed in a round bottomed
192 flask and, under vigorous stirring, a cold solution of NaBH_4 (0.081 mg, 2.133 mmol, 14.5 eq) in
193 deoxygenated water (3.9 mL) was quickly added. After stirring for 15 min at room temperature, a
194 dark red-violet dispersion of nanoparticles in chloroform was obtained. The aqueous phase was
195 discarded and the organic solution was divided equally in two flasks.

196 To the first sample a solution of thiol **3** (0.007 g, 0.025 mmol) in 3.3 mL of 2:1:0.3 deoxygenated
197 methanol:isopropanol:DMF was added dropwise to the nanoparticles solution in chloroform. The
198 suspension was stirred for 1.20 h at r.t. After wash with chloroform (4 x 20 mL) and ethanol (3 x
199 20 mL) and centrifugation at 4200 rpm for 5 min, nanoparticles were dried under flux of argon
200 and characterized. Nanoparticles are soluble in water. TEM: 4.1 ± 1.0 nm, $n = 557$. DLS: D_H 6.69
201 ± 2.05 nm. TGA: 15,3%. Average composition: $\text{Au}_{2600}\text{MDDS}_{330}$.

202 *Synthesis of NP4*: $\text{HAuCl}_4 \cdot x\text{H}_2\text{O}$ (0.100 g, 0.294 mmol, 1 eq) was dissolved in 11.6 mL of
203 deoxygenated water and stirred for 30 min at 25 °C with a solution of TOAB (0.869 g, 1.59 mmol,
204 5.4 eq) in 8.8 mL of deoxygenated chloroform.

205 After the colorless aqueous layer was discarded and a cold solution of NaBH_4 (0.161 mg, 4.27
206 mmol, 14.5 eq) in 7.8 mL deoxygenated water was quickly added to the orange organic phase
207 containing gold and the mixture was vigorously stirred for 15 min at 25°C. Finally, the aqueous
208 layer was removed and a dark red-violet solution of nanoparticles in chloroform was obtained.
209 0.013 g (0.036 mmol) of thiol **4** were dissolved in 8 mL of deoxygenated 3:1 methanol:isopropanol
210 mixture, and the obtained solution was added dropwise to the nanoparticles solution. After stirring

211 for 1.20 h at 25 °C, precipitated nanoparticles were washed by centrifugation with chloroform
212 pretreated with K₂CO₃ (5 x 20 mL) and methanol (5 x 20 mL). The obtained nanoparticles were
213 characterized by ¹H-NMR spectroscopy, TEM and UV-vis spectroscopy. The obtained
214 nanoparticles are soluble in water with 10% of isopropanol. TEM: 4.4 ± 1.0 nm, n = 550. DLS:
215 D_H 14.86 ± 4.25 nm. TGA 16%. Average composition: Au₂₉₅₀MHDS₃₈₄.

216 *Synthesis of NP5*: A solution of TOAB (0.084 g, 5.4 eq) in chloroform (7.6 mL) was added, under
217 argon atmosphere, to an aqueous solution of tetrachloroauric acid (0.084 g, 0.247 mmol, 1 eq) in
218 10 mL of deoxygenated milliQ water, at 25 °C and the reaction was let to stir for 15 minutes. The
219 two phases were separated and a solution of sodium borohydride (0.135 g, 3.58 mmol, 14.5 eq) in
220 11.5 mL of water was added to the organic phase. The red colored solution was stirred for 15
221 minutes and then a solution of thiol **5** (0.016 mg, 0.042 mmol) in 6.9 mL isopropanol was added.
222 The nanoparticles precipitated and the dispersion was stirred for 2 hours. The precipitate was
223 separated and washed five times with chloroform (30 mL, 4500 rpm, 5 min). TEM: 4.4 ± 0.9 nm,
224 n = 313. DLS: D_H 6.30 ± 0.92 nm. TGA: 18%. Average composition: Au₃₀₀₀ZW-PN₃₆₀.

225 *Computational methods*: Preparation and simulation of each nanoparticle model followed the
226 protocol described in our previous work^[52] and reported here in brief. Ligand **1-6** were prepared
227 using antechamber and assigning gaff2 atom types,^[61,62] force field parameters for the radical probe
228 were taken from the works of Barone et al.^[63,64]. Partial charges were calculated applying the RESP
229 method provided by RED^[65] server. Au-Au interactions were described with the parameters of
230 INTERFACE^[66] force field for metals. Icosahedral gold cores were built matching the
231 experimental values and the proper number of ligands was then assigned for the functionalization.
232 A harmonic bond was created between each sulfur atom and a gold atom within 3.3 Å with a spring
233 constant 50.000 kJ/mol*nm².^[67] Although this interface structure disregards possible gold–sulfur

234 binding motifs, it has been shown recently^[67] that this simplified treatment yields a description of
235 the structure of self-assembled alkanethiols of various length ($n = 3-15$) on 2-6 nm size gold core
236 in agreement with experiments. The systems were then solvated with TIP3P water molecules,
237 extending at least 15 Å from each solute atom, and counterions added to neutralize the system. A
238 combination of steepest descent (10000 cycles) and conjugate gradient (10000 cycles), followed
239 by a heating phase of 100 ps in NVT ensemble (integration step = 1 fs), was carried out to reach
240 the production temperature of 300 K. Then, density was brought to its final value with at least 50
241 ns in NPT conditions (integration step = 2 fs, pressure 1 atm), and pressure was maintained by
242 Berendsen barostat. Finally, we switched to Monte Carlo barostat for production run, of which the
243 first part was discarded until steady-state of ligands RMSD was reached. Trajectory for final
244 ensemble averages (400 ns) was stored from this point on. Temperature was controlled by
245 Langevin method (damping coefficient of 5 ps⁻¹) throughout all simulations. Electrostatic
246 interactions were computed by means of Particle Mesh Ewald (PME) algorithm, and calculations
247 were carried out using AMBER 18.^[68-71] Analysis was conducted using AMBERTools18 and in-
248 house Python scripts. Results were ensemble averaged on three repeated calculations. For systems
249 containing the probe, the radical was placed close to the equilibrated monolayer (not in contact)
250 changing initial position and orientation of the probe with respect to the NP and assigning different
251 starting velocities to enhance the sampling of the binding for a total of 1.6 μs time of simulation.
252 Further details are provided in the SM.

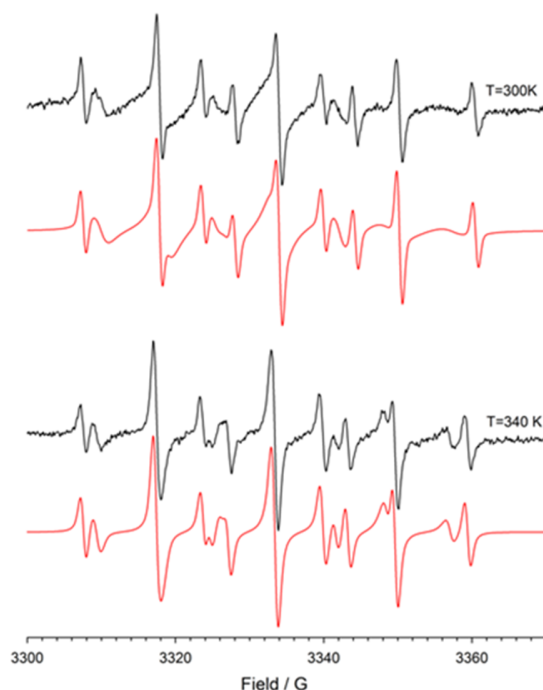
253

254 **3. Results and discussion**

255 **3.1. Ligand packing is sensitive to the size and hydrogen bonding capability of the end-group**

256 The ESR spectra of the radical probe were characterized by two resolved set of signals, see for
257 **NP1 Figure 3** as an example. The one with larger hyperfine coupling constants is due to the radical

258 located in water, while the second one arises from the radical hosted in the less polar environment
 259 of the monolayer, in equilibrium with the free nitroxide (see **Figure 1**), and has a nitrogen
 260 hyperfine splitting (a_N , see **Table 1**) significantly smaller than that measured for the radical in
 261 solution.
 262



263
 264 **Figure 3.** ESR spectra of the radical probe recorded in the presence of **NP1** (13.5 mg/0.1 mL) at
 265 300 K (top) and 340 K (bottom) in water. In red are reported the corresponding theoretical
 266 simulations, NRMSD (normalized root mean square displacement, RMSE/data range) 0.024 at 300
 267 K and 0.028 at 340 K.

268 **Table 1.** Spectroscopic parameters for the radical probe and partition equilibrium (K_{eq}) constants.
 269

NP	T (K)	a_N (G)	a_{2H} (G)	K_{eq} (M^{-1})
-	300	16.25	10.14	
-	340	16.22	9.80	
NP1	300	15.20	8.50	131
NP1	340	15.34	8.46	30
NP2	300	14.50^a	8.45^a	
NP2	300	15.18 ^b	8.58 ^b	
NP2	340	15.15	8.50	320
NP3	300	15.15	8.40	133

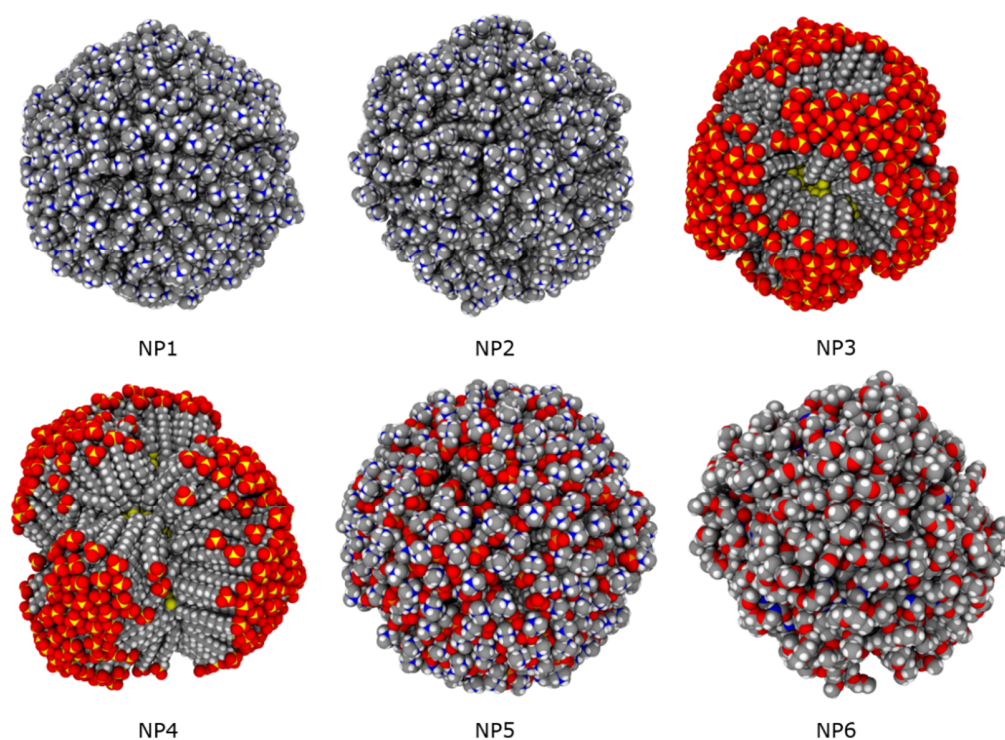
NP3	340	15.40	8.48	26
NP4	300	14.40^a	8.38^a	
NP4	300	15.23 ^b	8.30 ^b	
NP4	330	14.58^a	8.40^a	
NP4	330	15.33 ^b	8.33 ^b	
NP4	340	15.32	8.40	98
NP5	300	15.25	8.35	550
NP6^c	298	15.70	9.00	77

270 ^{a)} The values given in bold type refer to probe in the most hydrophobic location. ^{b)} These values refer to the
 271 less hydrophobic location of the probe. ^{c)} Data from ref. [56].

272 The spectroscopic parameters of the radical in the monolayer were very similar for **NP1**, **NP3** and
 273 **NP5** with a_N in the range of 15.15 – 15.25 G (**Table 1**), suggesting that the probe is experiencing
 274 a similar polarity even in presence of differently charged end groups. Surprisingly, these a_N values
 275 are 0.55 – 0.45 G units smaller than the corresponding value measured in previous works, when
 276 the same radical probe is immersed in the monolayer of ligand **6** (**NP6**, $a_N = 15.7$ G),^[56] and even
 277 smaller than those measured in fluorinated monolayers.^[58] This observation reflects a higher
 278 hydrophobicity experienced by the probe in the monolayer of **NP1**, **NP3** and **NP5** compared to
 279 **NP6**. Such behaviour was unexpected especially for **NP3** and **NP5**, where the probe hydroxyl
 280 moiety could, in principle, form hydrogen bonds with the oxygen atoms of sulfonate groups in
 281 **NP3** or with the oxygen of phosphate groups in **NP5**, thus bringing the nitroxide moiety of the
 282 probe more exposed to the aqueous medium and leading to an a_N value close to that measured for
 283 **NP6**.

284 At molecular level, MD calculations showed that in **NP6** ligands organize radially around the
 285 core (**Figure 4**), stabilized by the presence of interchain and chain/water hydrogen bonds (**Figure**
 286 **S1a** and **Table S1**). This is consistent with the disordered bent conformation of the PEG-end group
 287 and the presence of interligand C=O \cdots H-N hydrogen bonds as suggested by Rotello on the basis
 288 of IR measurements^[72] and more recently by Mancin and De Vivo,^[73,74] which also provide a
 289 degree of asphericity to the monolayer (**Table S2**). In agreement with the ESR data, the radical

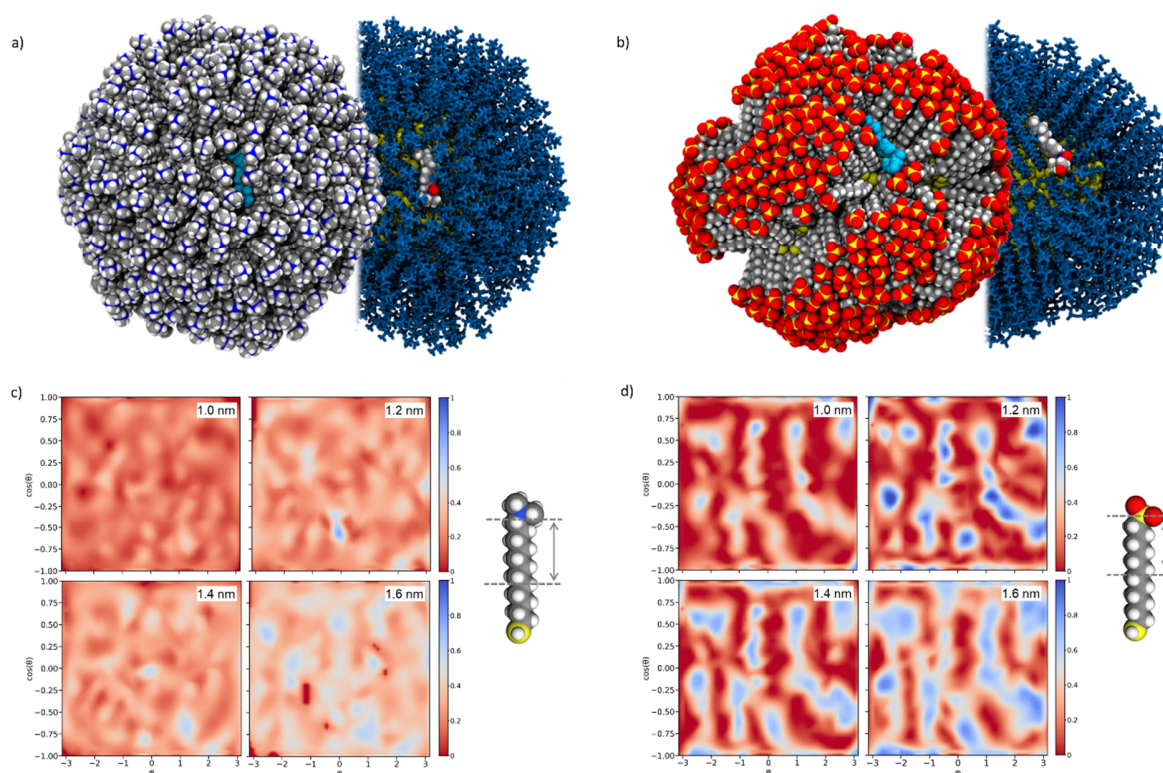
290 probe is completely immersed within the monolayer and oriented with the polar head in the
291 hydrophilic outer layer and the *para*-alkyl tail in the hydrophobic inner region (**Figure S2a**).
292 Radial distribution function (RDF) of the nitrogen atom of the probe allowed determining its
293 average position, which is centered at 1.28 nm (*N*-peak) distant from the gold surface, where it is
294 surrounded by a relatively hydrated environment (**Figure S2b** and **c**).



295
296 **Figure 4.** Space-filling model of monolayer organization around the NP gold core as obtained
297 from MD calculations for **NP1-NP6**. Solvent is not shown for clarity. Color legend: carbon, grey;
298 oxygen, red; sulfur, yellow; phosphorous, orange; nitrogen, blue; hydrogen, white.

299
300 By contrast, at 300 K, when **NP1** and **NP3** are considered, the nitrogen atom of the probe is located
301 at 1.46 and 1.34 nm (**Figure S3**), respectively, from the surface with its axis almost perpendicular
302 to the ligands axis (**Figure 5**). While **NP1** shows an isotropic distribution of ligands around the
303 core and a spherical shape, chains in **NP3** associate in more elongated bundles with almost all

304 chains in *trans* conformation (**Figure 4** and **Table S2**); thus, it appears that the sulfonate end-group
 305 with its less bulky nature allows ligands to better compact and order themselves establishing
 306 favourable interchain interactions. At the same time, ligands may be kept close by forming water
 307 bridges and hydrogen bonds with water molecules, which relief the electrostatic repulsion between
 308 the sulfonate groups (**Table S1** and **Figure S1b**).



309
 310 **Figure 5.** Binding of the radical probe within **NP1** (a, left) and **NP3** (b, left) in space-filling model.
 311 Solvent is not shown for clarity. Color code: probe, cyan; carbon, grey; oxygen, red; sulfur, yellow;
 312 nitrogen, blue; hydrogen, white. The probe is colored by atomic element (carbon, grey; nitrogen,
 313 blue; oxygen, red; hydrogen, white) in each right side of panel a/b, and the monolayer is depicted
 314 as blue sticks. Normalized water distribution at increasing distance from the gold surface for **NP1**
 315 (c) and **NP3** (d). The graphs plot the distribution of the atom (oxygen of water or carbon of
 316 thiolates) closest to gold surface (centered on the gold core and placed at increasing distances from
 317 its surface) shown as a two-dimensional projection of the sphere surface (x-axis, the azimuthal
 318 angle φ ; y-axis, the cosine of the polar angle θ). Value of 1 indicates that an oxygen atom of a
 319 water molecule is always the closest; if it is equal to 0, it indicates that a carbon atom of a chain
 320 is always the closest. Simplifying, red to salmon areas represent poorly hydrated zones, while blue
 321 areas stand for highly hydrated parts of the monolayer (at a certain distance from the gold surface).
 322 At distances lower than those considered the microenvironment is almost hydrophobic, while at

323 higher distances it is fully hydrated and no major difference between the monolayers could be then
324 detected. For bundled monolayer morphologies as in **NP3**, red areas are mainly constituted by
325 space points belonging to ligand bundles. The arrow superimposed to ligand **1** (c) and **3** (d)
326 structure helps to identify visually the region within the monolayer which the water maps refer to.
327

328 Despite thiols **1** and **3** have a comparable hydrophobic portion, the presence of a bulky end-group
329 and steric hindrance effect, in the former, forces the monolayer to adopt a radial organization.
330 Consequently, the probe is located isotropically inside the shell in the monolayer of **NP1** (**Figure**
331 **5a**), whereas in **NP3** it binds the monolayer at bundle interface, deep in the valley between bundles
332 (**Figure 5b**).

333 Interestingly, regardless the different monolayer organization and interaction position, the probe
334 shares in **NP1** and **NP3** a similar hydration environment as identified from water density
335 distribution at radial distances close to the average nitrogen position of the probe (compare **Figure**
336 **5c** and **5d**). This provides a molecular interpretation of the similarity in the spectroscopic
337 parameters $a_{\text{N}}(G)$, $a_{2\text{H}}(G)$ found in the ESR measurements. Furthermore, the averaged hydration
338 values around the nitrogen atom of the probe in **NP1** or **NP3** are much lower compared to that in
339 **NP6**, supporting higher hydrophobicity of these two monolayers compared to monolayer of ligand
340 **6** in agreement with ESR data in **Table 1**.

341 For **NP5** MD simulations predicted a radial organization of the chains (**Figure 4**) and the
342 nanoparticle adopts a spherical shape with a slightly lower fraction of *trans* dihedrals respect to
343 **NP1** (**Table S2**). The thickness of the self-assembled monolayer, obtained from XPS data
344 according to the methodology described by Shard,^[75] is of 1.37 nm (see SM for further details on
345 the methodology), in good agreement with the computational average value of 1.58 nm, supporting
346 the folding at the phosphate group, which exposes both ions to water. Also in this case, the presence
347 of bulky end groups hinders ligand association in long-living bundles. The radial conformation is

348 stabilized by a significant amount of hydrogen bonds, both involving ligand-water and ligand-
349 water-ligand interactions (**Table S1** and **Figure S1c**). This induces a stable hydration network in
350 the outer layer of the shell, and hampers further solvent penetration as it can be clearly assessed
351 by comparing solvent density distributions for **NP5** and **NP1** systems (**Figure S4c** and **5c**). At the
352 same distance from the gold core, the monolayer of **NP5** appears much less hydrated than **NP1**.
353 The probe is mainly placed 1.55 nm far from the gold surface (**Figure S4b**), where the average
354 water distribution is comparable to that observed close to the *N*-peak in **NP1** and **NP3**, thus
355 explaining the similarity of the spectroscopic parameters for these systems.

356 As expected, hydrogen bond formation between the probe and the oxygen atoms of the phosphate
357 is detected; however, these bonds exist only for 67% of the simulation time, which is lower than
358 the 80% calculated for **NP6** (**Figure S5**). Taken together, these evidences justify the unexpected
359 lower value of a_N of **NP5** compared to **NP6**.

360

361 **3.2 The probe is hosted in a complex environment in thicker monolayers and binding is** 362 **maximized by zwitterionic end-groups**

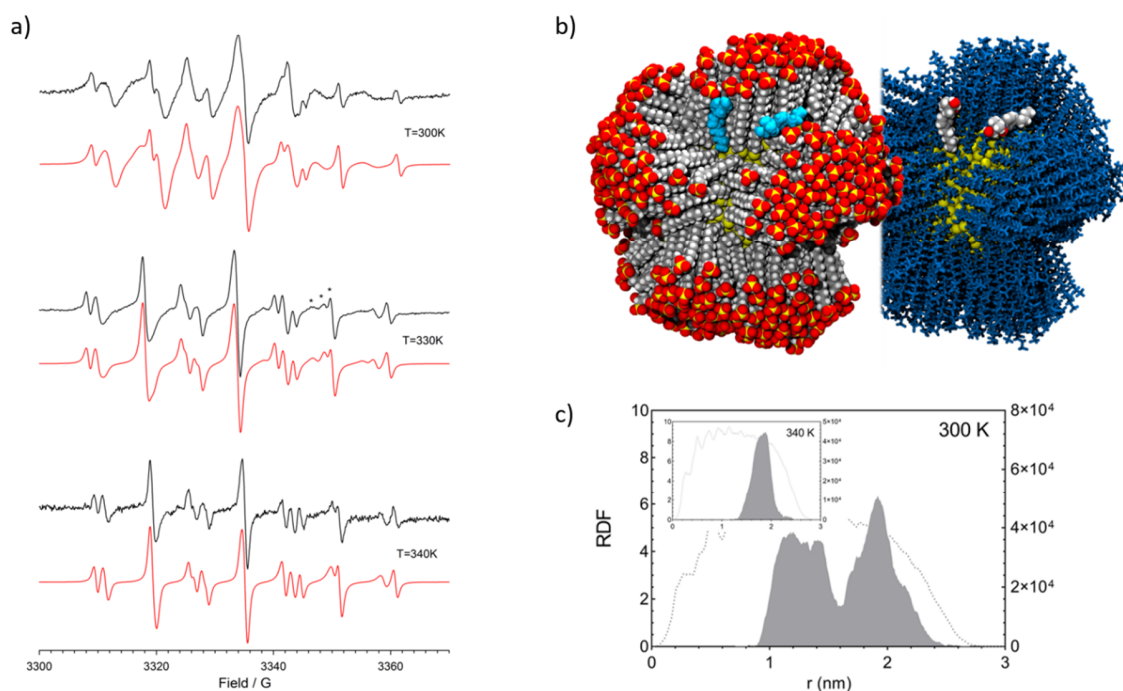
363 A different behaviour was instead observed in presence of monolayers composed of longer
364 hydrocarbon chains containing 16 carbon atoms, i.e. **NP2** and **NP4**. **Figure 6a** shows the ESR
365 spectrum of the nitroxide probe recorded at 300 K in the presence of **NP4**. The spectrum of the
366 radical probe is characterized by the presence of two set of signals due to the radical hosted in the
367 less polar environment of AuNP monolayer, in equilibrium with the free nitroxide.

368 However, comparison of the values of a_N for the radical located in the longer **NP4** and shorter
369 **NP3** monolayer indicates that it is substantially smaller (in Gauss equal to -0.70) in the former
370 case (**Table 1**). This suggests that the probe in **NP4** is positioned in an environment having a

371 polarity lower than that experienced in the shorter chain monolayer of **NP3**, hereafter named
372 **probe@position1**.

373 By increasing the temperature, a new set of signals, characterized by spectroscopic parameters
374 very similar to those previously measured in the monolayer of **NP3** appears in the spectrum, named
375 **probe@position2** (**Figure 6a**, 330 K, and **Table 1**). The presence of this new triplet of triplets is
376 indicative of two diverse sites where the radical is located in the monolayer experimenting different
377 polarities.

378



379

380 **Figure 6.** a) ESR spectra of the radical probe recorded in the presence of **NP4** (13.3 mg/0.1mL) at
381 300 K (top), 330 K (middle) and 340 K (bottom). Stars refer to the three different radical species
382 (see text). In red are reported the corresponding theoretical simulations; NRMSD: 0.035 at 300 K,
383 0.0164 at 330 K and 0.044 at 340 K. b) Representative binding mode of the radical probe within
384 **NP4 @position1** and **@position2** from MD simulations at 300 K in space-filling model. Color
385 code: probe, cyan; carbon, grey; oxygen, red; sulfur, yellow; hydrogen, white. Positions are
386 superimposed to allow visual comparison. The probe is also reported by atomic element (carbon,
387 grey; nitrogen, blue; oxygen, red; hydrogen, white) in the right side of panel (b), and the monolayer

388 is depicted as blue sticks. c) MD radial distribution function (RDF) of nitrogen atom of the radical
389 probe in the monolayer of **NP4** at 300 K (solid line, left axis) and ligand **4** (dotted line, right axis)
390 reported from the gold surface. Inset: same RDFs as in panel c), but predicted at 340 K.

391
392 The relative concentration of the probe in these two positions changes reversibly varying the
393 temperature, being **probe@position2** the dominant species at higher temperatures (340 K, **Figure**
394 **6a**). Thus, we were able to reproduce the experimental spectra by considering different amount of
395 the radical specie located in the three different environments at different temperatures in the
396 corresponding theoretical simulations (see red line in **Figure 6a**). The quantitative determination
397 of the relative amounts of the radical in the different positions, however, was drastically hampered
398 by the poor spectral resolution and only a crude estimation of
399 $[\text{probe@position1}]/[\text{probe@position2}]$ ratio was possible. On this basis, we estimated a
400 $[\text{probe@position1}]/[\text{probe@position2}]$ ratio equal to ≈ 0.3 and ≈ 2.7 at 300 and 330 K,
401 respectively. Van't-Hoff plot of these data (**Figure S6**), gives rise to approximate thermodynamic
402 parameters $\Delta H = +13 \pm 4$ kJ/mol, $\Delta S = +42 \pm 12$ Jmol⁻¹ K⁻¹, indicating an entropy driven
403 equilibrium for the formation of the **probe@postion2** at higher temperatures.

404 At molecular level, the long ligand **4** assembled into five bundles, which endow the NP with a
405 less rounded structure (**Figure 4** and **Table S2**); as also seen in **NP3**, ligand-water-ligand hydrogen
406 bonds take place between the oxygen atoms of the sulfonate end group, contributing to chain
407 compaction and ligand ordering (**Table S1** and **S2**). The radical probe interacts with **NP4** shell at
408 the energetically-favoured interface between the bundles (**Figure 6b**) and at 300 K the *N*-peak is
409 found at two main distinct locations in contact with the monolayer (**Figure 6c**): the first at 1.26
410 nm and the second at 1.90 nm from the gold surface, in agreement with experimental ESR data.
411 These positions are characterized by a significantly different hydration. As shown in **Figure S7**,

412 at a distance of 1.26 nm from the core, a limited number of water molecules access the monolayer
413 and the environment is virtually hydrophobic, this corresponding to the **probe@position1** detected
414 by ESR. Moving to 1.90 nm, the probe enters a much more hydrophilic local environment. At
415 higher temperatures (340 K), the two peaks merge in one single peak with an average *N* position
416 at 1.83 nm from the metal surface (**Figure 6c**, inset), which resembles **probe@position2**.

417 Similar experimental results were also obtained with **NP2**. In this case, however, the spectral
418 resolution and the differences in the value of hyperfine splitting constants did not permit to
419 spectroscopically resolve the signals of the radicals partitioned in the two different monolayer
420 environments. It is interesting to note that the larger affinity of the probe for **NP2** monolayer
421 allowed us to record spectra containing mainly the signal due to **probe@position1** at 300 K and
422 **probe@position2** at 340 K (see **Figure S8**).

423 MD simulations show that despite **NP2** exhibits a uniform radial organization of ligands around
424 the core (**Figure 4**) thanks to the large trimethylammonium end group, two distinct probe locations
425 were found at 300 K (**Figure S9a**); the first, with the *N*-peak at 1.02 nm from Au surface and
426 poorly hydrated, corresponds to the low-polarity **probe@position1**. The second, placed at 1.64
427 nm, is more hydrated and well describes **probe@position2** (**Figure S9b**). The peaks merge in one
428 single peak at 340 K (1.83 nm) (**Figure S9a**). XPS data acquired on **NP2** support these outcomes,
429 returning a thickness of the organic shell around the metal core of ca. 1.88 ± 0.10 nm (see SM)
430 indicative of a fully extended alkyl chain, which agrees well with the high percentage of *trans*
431 dihedrals in the ligand chains (**Table S2**).

432 Thus, sufficiently long ligand chains allow the probe to bind in two distinct sites, not observed
433 in monolayers composed of shorter ligands, one located deeper in the shell and the other more
434 exposed to the exterior.

435 Relevant is the analysis of K_{eq} values measured by ESR (**Table 1**), which is also consistent with
436 the monolayer packing picture offered by MD simulations. In general, the partition equilibrium
437 constants are lower at higher temperature as expected from the thermodynamics of the process and
438 increase with the thickness of the hydrophobic portion of the monolayer up to one order of
439 magnitude, see data for **NP1** vs. **NP2** and **NP3** vs. **NP4** in **Table 1**. Moreover, the presence of
440 open canyons allows easier ingoing and outgoing of the probe compared to radial monolayers, and
441 is consistent with the lower K_{eq} measured for **NP4** with respect to **NP2**. Additionally, the
442 zwitterionic monolayer in **NP5** favours the complex formation by a factor of 4 with respect to **NP1**
443 and **NP3**, presenting the same hydrophobic monolayer thickness.

444

445 **4. Conclusions**

446 Experimental ESR studies combined with MD simulations suggest that the packing mode of self-
447 assembled monolayers on gold nanoparticles with a core of ~ 4 nm is affected by the nature and
448 space occupied by ligand end group. Larger size surface groups such as trimethylammonium,
449 zwitterionic and PEG groups, lead to a radial organization and the end-group contribution
450 overcomes association-promoting interactions, as van der Waals and solvophobic forces. On the
451 contrary, smaller end-groups, such as sulfonate ones, allow chains to arrange closer and establish
452 further stabilizing interactions (such as hydrogen bonds), which cooperate to make ligand bundles
453 long-living. This has significant consequences on hydration of the monolayer, local environment
454 and solvent distribution within the shell, which is more uniform in radially organized than
455 anisotropic monolayers.

456 Another key finding is that for long enough chains two positions at distinct polarity exist, where
457 a hydrophobic host could be detected, opening to the design of monolayers able to promote

458 catalytic events influenced by the number of water molecules present in the catalytic site, similarly
459 to enzymes.

460 Thus, the role of the end-group is not limited to the surface properties but its nature influences
461 structure and hydration of the whole self-assembled monolayer. This study reveals that one,
462 simple, molecular-level parameter (chemical nature and size of NP surface group) affects the
463 monolayer properties across several length scales, from molecular- up to nano-scale.

464 We trust that this work will offer novel perspectives on the molecular features controlling the
465 behaviour of SAM protected gold nanoparticles, their ability to host hydrophobic drugs and
466 interface with exogenous molecules as nanocarriers or nanoreceptors with tailored affinity and
467 selectivity.

468

469 **Supporting Material**

470 Synthesis and characterization of thiols and characterization of nanoparticles. ESR experimental
471 details. XPS characterization of monolayer-protected nanoparticles. Additional results.

472

473 **Acknowledgements**

474 This research was supported by the Italian Ministry of University Research through the projects
475 PRIN2017 NiFTy (2017MYBTXC to L.P.), “Structure and function at the nanoparticle
476 biointerface” (RBSI14PBC6 to P.P.), (2017E44A9P to M. L.), by the University of Trieste (FRA
477 2018 to L.P.) and by the Jan Evangelista Purkyně University (grant No. UJEP-IGA-TC-2019-53-
478 02-2 to Z. P.). CERIC-ERIC consortium is acknowledged for the access to the Material Science
479 beamline at the Elettra synchrotron radiation facility (proposal number 20192081). Prof.
480 Alessandro Baraldi is kindly acknowledged for very helpful suggestions and discussion for XPS

481 measurements and data analysis. We thank Cristian Gabellini for instructive suggestions on data
482 manipulation.

483 **Author contribution**

484 E.P. and M.Ş. made the synthesis/purification and the basic characterization of gold nanoparticles;
485 M.Ş. contributed to the writing of the experimental part of synthesis and characterization; M.D.
486 contributed to samples characterization and XPS measurements; P.Pengo contributed to the
487 characterization of gold nanoparticles, supervised the synthetic work, participated to general
488 discussion and contributed to the first draft of the manuscript; D.M. optimized the molecular
489 models and carried out MD analysis; D.M. and Z.P. performed MD calculations; S.F. and L.B
490 performed XPS data acquisition; L.B. supervised XPS experiments, elaborated XPS data, and
491 contributed to the writing of the manuscript; P.F. contributed to ESR measurements; M.L.
492 supervised ESR experiments, elaborated ESR data, participated to general discussion; P.Posocco
493 supervised MD simulations and data analysis; L.P. and P.Posocco conceived the project; L.P.
494 coordinated all contributions; L.P., P.Posocco and M.L. analyzed and discussed the results and
495 contributed to writing the manuscript and prepared the final version.

496

497 **Conflict of Interest**

498 There are no conflicts to declare.

499

500

501 **References**

- 502 [1] J. R. Banavar, T. J. Cooke, A. Rinaldo, A. Maritan, *Proc. Natl. Acad. Sci.* **2014**, *111*, 3332.
- 503 [2] D. W. Sanders, N. Kedersha, D. S. W. Lee, A. R. Strom, V. Drake, J. A. Riback, D.
- 504 Bracha, J. M. Eeftens, A. Iwanicki, A. Wang, M. T. Wei, G. Whitney, S. M. Lyons, P.
- 505 Anderson, W. M. Jacobs, P. Ivanov, C. P. Brangwynne, *Cell* **2020**, *181*, 306.
- 506 [3] Z. Liu, X. Han, R. Chen, K. Zhang, Y. Li, S. Fruge, J. H. Jang, Y. Ma, L. Qin, *ACS Appl.*
- 507 *Mater. Interfaces* **2017**, *9*, 22143.
- 508 [4] C. Luschnig, G. Vert, *Development* **2014**, *141*, 2924.
- 509 [5] J. Zhao, M. H. Stenzel, *Polym. Chem.* **2018**, *9*, 259.
- 510 [6] S. Shinoda, H. Tsukube, *Chem. Sci.* **2011**, *2*, 2301.
- 511 [7] M. L. Bender, E. T. Kaiser, *J. Am. Chem. Soc.* **1962**, *84*, 2556.
- 512 [8] Y. Murakami, J.-I. Kikuchi, Y. Hisaeda, O. Hayashida, *Chem. Rev.* **1996**, *96*, 721.
- 513 [9] C. A. Bunton, F. Nome, F. H. Quina, L. S. Romsted, *Acc. Chem. Res.* **1991**, *24*, 357.
- 514 [10] Y. Murakami, Y. Hisaeda, X.-M. Song, T. Ohno, *J. Chem. Soc., Perkin Trans. 2* **1992**, *9*,
- 515 1527.
- 516 [11] J. T. Groves, R. Neumann, *J. Am. Chem. Soc.* **1989**, *111*, 2900.
- 517 [12] J. T. Groves, S. B. Ungashe, *J. Am. Chem. Soc.* **1990**, *112*, 7796.
- 518 [13] R. Ueoka, Y. Matsumoto, R. A. Moss, S. Swarup, A. Sugii, K. Harada, J. Kikuchi, Y.
- 519 Murakami, *J. Am. Chem. Soc.* **1988**, *110*, 1588.
- 520 [14] J. C. Love, L. A. Estroff, J. K. Kriebel, R. G. Nuzzo, G. M. Whitesides, *Chem. Rev.* **2005**,
- 521 *105*, 1103.
- 522 [15] M. De, P. S. Ghosh, V. M. Rotello, *Adv. Mater.* **2008**, *20*, 4225.
- 523 [16] J. Czescik, S. Zamolo, T. Darbre, R. Rigo, C. Sissi, A. Pecina, L. Riccardi, M. De Vivo, F.
- 524 Mancin, P. Scrimin, *Angew. Chem. Int. Ed.* **2021**, *60*, 1423.
- 525 [17] M. A. Boles, D. Ling, T. Hyeon, D. V. Talapin, *Nat. Mater.* **2016**, *15*, 141.
- 526 [18] N. D. Burrows, W. Lin, J. G. Hinman, J. M. Dennison, A. M. Vartanian, N. S. Abadeer, E.
- 527 M. Grzincic, L. M. Jacob, J. Li, C. J. Murphy, *Langmuir* **2016**, *32*, 9905.
- 528 [19] M. Wu, A. M. Vartanian, G. Chong, A. K. Pandiakumar, R. J. Hamers, R. Hernandez, C. J.
- 529 Murphy, *J. Am. Chem. Soc.* **2019**, *141*, 4316.
- 530 [20] F. P. Cometto, Z. Luo, S. Zhao, J. A. Olmos-Asar, M. M. Mariscal, Q. Ong, K. Kern, F.
- 531 Stellacci, M. Lingenfelder, *Angew. Chem. Int. Ed.* **2017**, *56*, 16526.

- 532 [21] C. Weeraman, A. K. Yatawara, A. N. Bordenyuk, A. V. Benderskii, *J. Am. Chem. Soc.*
533 **2006**, *128*, 14244.
- 534 [22] W. Edwards, N. Marro, G. Turner, E. R. Kay, *Chem. Sci.* **2018**, *9*, 125.
- 535 [23] P. U. Atukorale, Z. P. Guven, A. Bekdemir, R. P. Carney, R. C. Van Lehn, D. S. Yun, P.
536 H. Jacob Silva, D. Demurtas, Y.-S. Yang, A. Alexander-Katz, F. Stellacci, D. J. Irvine,
537 *Bioconj. Chem.* **2018**, *29*, 1131.
- 538 [24] S. Sabella, R. P. Carney, V. Brunetti, M. A. Malvindi, N. Al-Juffali, G. Vecchio, S. M.
539 Janes, O. M. Bakr, R. Cingolani, F. Stellacci, P. P. Pompa, *Nanoscale* **2014**, *6*, 7052.
- 540 [25] D. Marson, F. Guida, M. Şologan, S. Boccardo, P. Pengo, F. Perissinotto, V. Iacuzzi, E.
541 Pellizzoni, S. Polizzi, L. Casalis, L. Pasquato, S. Pacor, A. Tossi, P. Posocco, *Small* **2019**,
542 *15*, 1900323.
- 543 [26] M. Şologan, C. Cantarutti, S. Bidoggia, S. Polizzi, P. Pengo, L. Pasquato, *Faraday*
544 *Discuss.* **2016**, *191*, 527.
- 545 [27] A. Centrone, E. Penzo, M. Sharma, J. W. Myerson, A. M. Jackson, N. Marzari, F.
546 Stellacci, *Proc. Natl. Acad. Sci.* **2008**, *105*, 9886.
- 547 [28] D. F. Moyano, Y. Liu, D. Peer, V. M. Rotello, *Small* **2016**, *12*, 76.
- 548 [29] P. Pengo, M. Şologan, L. Pasquato, F. Guida, S. Pacor, A. Tossi, F. Stellacci, D. Marson,
549 S. Boccardo, S. Pricl, P. Posocco, *Eur. Biophys. J.* **2017**, *46*, 749.
- 550 [30] M. D. Manning, A. L. Kwansa, T. Oweida, J. S. Peerless, A. Singh, Y. G. Yingling,
551 *Biointerphases* **2018**, *13*, 06D502.
- 552 [31] F. Muraca, L. Boselli, V. Castagnola, K. A. Dawson, *ACS Appl. Bio Mater.* **2020**, *3*, 3800.
- 553 [32] L. Boselli, E. Polo, V. Castagnola, K. A. Dawson, *Angew. Chem. Int. Ed.* **2017**, *56*, 4215.
- 554 [33] M. Siek, K. Kandere-Grzybowska, B. A. Grzybowski, *Acc. Mater. Res.* **2020**, *1*, 188.
- 555 [34] P. D. Jadzinsky, G. Calero, C. J. Ackerson, D. A. Bushnell, R. D. Kornberg, *Science* **2007**,
556 *318*, 430.
- 557 [35] C. Zeng, Y. Chen, K. Kirschbaum, K. J. Lambright, R. Jin, *Science* **2016**, *354*, 1580.
- 558 [36] Y. Li, T. Higaki, X. Du, R. Jin, *Adv. Mater.* **2020**, *32*, 1905488.
- 559 [37] E. Colangelo, J. Comenge, D. Paramelle, M. Volk, Q. Chen, R. Lévy, *Bioconj. Chem.*
560 **2017**, *28*, 11.
- 561 [38] P. K. Ghorai, S. C. Glotzer, *J. Phys. Chem. C* **2007**, *111*, 15857.
- 562 [39] D. S. Bolintineanu, J. M. D. Lane, G. S. Grest, *Langmuir* **2014**, *30*, 11075.

- 563 [40] A. K. Giri, E. Spohr, *J. Phys. Chem. C* **2018**, *122*, 26739.
- 564 [41] P. Posocco, C. Gentilini, S. Bidoggia, A. Pace, P. Franchi, M. Lucarini, M. Fermeglia, S.
565 Pricl, L. Pasquato, *ACS Nano* **2012**, *6*, 7243.
- 566 [42] M. Şologan, D. Marson, S. Polizzi, P. Pengo, S. Boccardo, S. Pricl, P. Posocco, L.
567 Pasquato, *ACS Nano* **2016**, *10*, 9316.
- 568 [43] Z. Luo, D. Marson, Q. K. Ong, A. Loiudice, J. Kohlbrecher, A. Radulescu, A. Krause-
569 Heuer, T. Darwish, S. Balog, R. Buonsanti, D. I. Svergun, P. Posocco, F. Stellacci, *Nat.*
570 *Commun.* **2018**, *9*, 1343.
- 571 [44] W. D. Luedtke, U. Landman, *J. Phys. Chem. B* **1998**, *102*, 6566.
- 572 [45] U. Landman, W. D. Luedtke, *Faraday Discuss.* **2004**, *125*, 1.
- 573 [46] A. Badia, W. Gao, S. Singh, L. Demers, L. Cuccia, L. Reven, *Langmuir* **1996**, *12*, 1262.
- 574 [47] H. Schmitt, A. Badia, L. Dickinson, L. Reven, R. B. Lennox, *Adv. Mater.* **1998**, *10*, 475.
- 575 [48] P. Fiurasek, L. Reven, *Langmuir* **2007**, *23*, 2857.
- 576 [49] M. Lucarini, P. Franchi, G. F. Pedulli, P. Pengo, P. Scrimin, L. Pasquato, *J. Am. Chem.*
577 *Soc.* **2004**, *126*, 9326.
- 578 [50] E. Ertem, M. Diez-Castellnou, Q. K. Ong, F. Stellacci, *Chem. Rec.* **2018**, *18*, 819.
- 579 [51] B. Perrone, S. Springhetti, F. Ramadori, F. Rastrelli, F. Mancin, *J. Am. Chem. Soc.* **2013**,
580 *135*, 11768.
- 581 [52] D. Marson, Z. Posel, P. Posocco, *Langmuir* **2020**, *36*, 5671.
- 582 [53] C. Pezzato, S. Maiti, J. L. Y. Chen, A. Cazzolaro, C. Gobbo, L. J. Prins, *Chem. Commun.*
583 **2015**, *51*, 9922.
- 584 [54] C. K. Kim, P. Ghosh, C. Pagliuca, Z.-J. Zhu, S. Menichetti, V. M. Rotello, *J. Am. Chem.*
585 *Soc.* **2009**, *131*, 1360.
- 586 [55] M. Boccalon, S. Bidoggia, F. Romano, L. Gualandi, P. Franchi, M. Lucarini, P. Pengo, L.
587 Pasquato, *J. Mater. Chem. B* **2015**, *3*, 432.
- 588 [56] M. Lucarini, P. Franchi, G. F. Pedulli, C. Gentilini, S. Polizzi, P. Pengo, P. Scrimin, L.
589 Pasquato, *J. Am. Chem. Soc.* **2005**, *127*, 16384.
- 590 [57] C. Gentilini, P. Franchi, E. Mileo, S. Polizzi, M. Lucarini, L. Pasquato, *Angew. Chem. Int.*
591 *Ed.* **2009**, *48*, 3060.
- 592 [58] C. Gentilini, F. Evangelista, P. Rudolf, P. Franchi, M. Lucarini, L. Pasquato, *J. Am. Chem.*
593 *Soc.* **2008**, *130*, 15678.

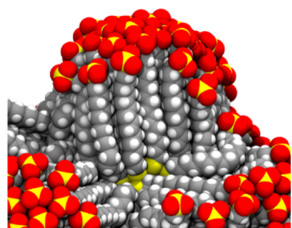
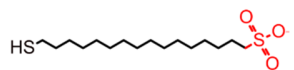
- 594 [59] S. Bidoggia, F. Milocco, S. Polizzi, P. Canton, A. Saccani, B. Sanavio, S. Krol, F.
595 Stellacci, P. Pengo, L. Pasquato, *Bioconj. Chem.* **2017**, 28, 43.
- 596 [60] T. R. Graham, R. Renslow, N. Govind, S. R. Saunders, *J. Phys. Chem. C* **2016**, 120,
597 19837.
- 598 [61] J. Wang, R. M. Wolf, J. W. Caldwell, P. A. Kollman, D. A. Case, *J. Comput. Chem.* **2004**,
599 25, 1157.
- 600 [62] J. Wang, W. Wang, P. A. Kollman, D. A. Case, *J. Mol. Graph. Model.* **2006**, 25, 247.
- 601 [63] V. Barone, A. Bencini, M. Cossi, A. D. Matteo, M. Mattesini, F. Totti, *J. Am. Chem. Soc.*
602 **1998**, 120, 7069.
- 603 [64] R. Improta, A. di Matteo, V. Barone, *Theor. Chem. Acc.* **2000**, 104, 273.
- 604 [65] E. Vanquelef, S. Simon, G. Marquant, E. Garcia, G. Klimerak, J. C. Delepine, P. Cieplak,
605 F.-Y. Dupradeau, *Nucleic Acids Res.* **2011**, 39, W511.
- 606 [66] H. Heinz, T.-J. Lin, R. Kishore Mishra, F. S. Emami, *Langmuir* **2013**, 29, 1754.
- 607 [67] A. K. Chew, R. C. Van Lehn, *J. Phys. Chem. C* **2018**, 122, 26288.
- 608 [68] D.A. Case, I.Y. Ben-Shalom, S.R. Brozell, D.S. Cerutti, I. T.E. Cheatham, V.W.D.
609 Cruzeiro, T.A. Darden, R.E. Duke, D. Ghoreishi, M.K. Gilson, H. Gohlke, A.W. Goetz, D.
610 Greene, R Harris, N. Homeyer, S. Izadi, A. Kovalenko, T. Kurtzman, T.S. Lee, S.
611 LeGrand, P. Li, C. Lin, J. Liu, T. Luchko, R. Luo, D.J. Mermelstein, K.M. Merz, Y. Miao,
612 G. Monard, C. Nguyen, H. Nguyen, I. Omelyan, A. Onufriev, F. Pan, R. Qi, D.R. Roe, A.
613 Roitberg, C. Sagui, S. Schott-Verdugo, J. Shen, C.L. Simmerling, J. Smith, R. Salomon-
614 Ferrer, J. Swails, R.C. Walker, J. Wang, H. Wei, R.M. Wolf, X. Wu, L. Xiao, D.M. York
615 and P. A. Kollman, AMBER 2018, University of California, San Francisco.
- 616 [69] R. Salomon-Ferrer, D. A. Case, R. C. Walker, *Wiley Interdiscip. Rev. Comput. Mol. Sci.*
617 **2013**, 3, 198.
- 618 [70] R. Salomon-Ferrer, A. W. Götz, D. Poole, S. Le Grand, R. C. Walker, *J. Chem. Theory*
619 *Comput.* **2013**, 9, 3878.
- 620 [71] S. Le Grand, A. W. Götz, R. C. Walker, *Comput. Phys. Commun.* **2013**, 184, 374.
- 621 [72] A. K. Boal, V. M. Rotello, *Langmuir* **2000**, 16, 9527.
- 622 [73] L. Riccardi, L. Gabrielli, X. Sun, F. De Biasi, F. Rastrelli, F. Mancin, M. De Vivo, *Chem*
623 **2017**, 3, 92.

- 624 [74] X. Sun, L. Riccardi, F. De Biasi, F. Rastrelli, M. De Vivo, F. Mancin, *Angew. Chem. Int.*
625 *Ed.* **2019**, *58*, 7702.
- 626 [75] A. G. Shard, *J. Phys. Chem. C* **2012**, *116*, 16806.
- 627
628
629

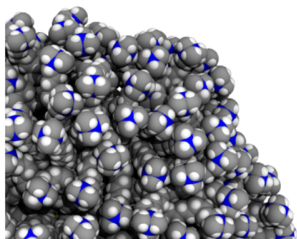
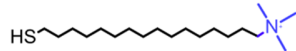
630
631
632
633

Graphical abstract

634



bundled SAM



urchin-like SAM